Projective measurements: Topological quantum computing with an arbitrary number of qubits

Themba Hodge, Philipp Frey, and Stephan Rachel*
School of Physics, The University of Melbourne, Parkville, VIC 3010, Australia

(Received 19 August 2025; accepted 14 July 2026; published 29 July 2026)

Topological quantum computing promises intrinsic fault tolerance by encoding quantum information in non-Abelian anyons, where quantum gates are implemented via braiding. While braiding operations are robust against local perturbations, a critical yet often overlooked challenge arises when scaling beyond two qubits: the naive extension of braiding-based gates fails to support even the full Clifford group. To overcome this limitation, we incorporate projective measurements that enable transitions between different qubit encodings, thus restoring computational universality. We perform many-body simulations of braiding dynamics augmented with measurement-based switching, explicitly preparing the Bell state and Greenberger–Horne–Zeilinger state for systems of two and five qubits, respectively. Furthermore, we execute a random unitary circuit on five qubits, achieving a fidelity exceeding 99%. We analyze the circuit's robustness by studying its fidelity dependence on total braid duration and static potential disorder. Our results show that the fidelity remains above 99% for moderate disorder, underscoring the intrinsic fault tolerance of the architecture. Finally, we demonstrate a random circuit on a ten-qubit system to showcase the scalability of our techniques.

DOI: 10.1103/5q9d-3dc7

I. INTRODUCTION

The advantage of topological quantum computation (TQC) lies in the implementation of quantum gates via braiding. The pairwise exchange of Majorana zero modes (MZMs) leads to an action on the degenerate many-body ground-state manifold that is identical to the action of a unitary operator on the Hilbert space that it spans [1–7]. In fact, for up to two qubits, all Clifford gates can be implemented via braiding [8]. Crucially, this implementation of quantum gates is inherently fault tolerant due to topological protection against local noise.

A major obstacle to the practical realization of TQC concerns the encoding of qubits using Majorana operators in a way that supports universal computation. In one-dimensional topological superconductors, two end-localized Majoranas define a nonlocal fermionic mode [9], with the vacuum and occupied states typically mapped to $|0\rangle$ and $|1\rangle$, respectively. However, qubit counting is nontrivial: $2N$ Majoranas do not yield N-independent qubits due to global fermion parity constraints, which reduce the accessible Hilbert space by half. This conservation law also blocks coherent superpositions of different parity sectors via braiding alone, limiting the ability to dynamically prepare arbitrary quantum states. Any solution to this problem involves the addition

*Contact author: stephan.rachel@unimelb.edu.au

Published by the American Physical Society under the terms of the Creative Commons Attribution 4.0 International license. Further distribution of this work must maintain attribution to the author(s) and the published article's title, journal citation, and DOI.

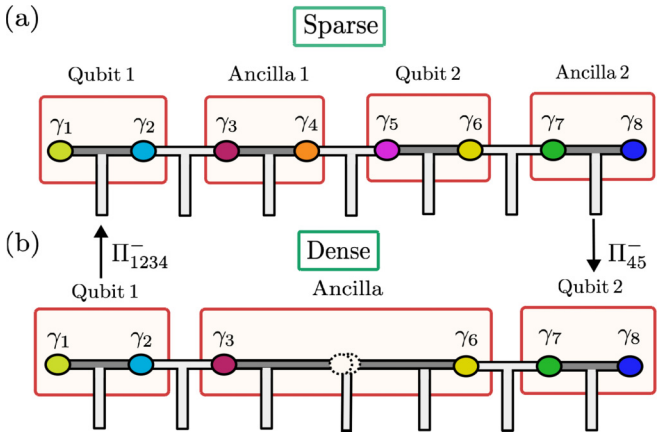


FIG. 1. Logical qubit encodings on T-junction geometry. (a) Sparse encoding for two qubits, each consisting of a physical and a parity-conserving ancilla qubit. (b) Dense encoding for two qubits, consisting of physical qubits and a single ancilla qubit. Note that γ_4 and γ_5 are absent from the dense encoding after the joint-parity measurement, highlighted by the hollow circles.

of auxiliary qubits [4,10]. This may be done in several different ways, each of which constitutes a particular *encoding*. However, it can be shown that no one encoding alone allows for universality if only braiding and hybridization between two Majoranas are considered.

Here, we utilize the *sparse* and *dense* encodings [10]. The sparse encoding assigns four Majoranas to each logical qubit, meaning that each qubit comes with its own ancillary, and allows for the implementation of all single-qubit Clifford gates via braiding of the four Majoranas. In addition, the famous magic gate may be implemented via hybridization, i.e., a controlled energy splitting induced by their mutual proximity [11–13]. The downside of this encoding is that different qubits cannot be entangled with one another. The dense encoding, on the other hand, assigns $2N + 2$ Majoranas to N logical qubits and therefore requires only one ancillary. It readily allows for mutual entanglement. However, the full set of single-qubit Clifford gates is available only on the first and the last logical qubit.

Unfortunately, this limitation has hampered classical simulation of TQC beyond two qubits. Previous works have been able to successfully simulate up to two qubits in the dense encoding [13–16]. To capture the full nonequilibrium dynamics of large quantum circuits, this gap in the literature *must* be filled to scale classical simulation methods far beyond two qubits on a universal gate set. This includes quantifying the inhibitive effects of Majorana hybridization [13,17], diabatic error [18–20], disorder [21–24], and quasiparticle poisoning [25–28] on physical devices in a full dynamical context.

The limitation of each encoding can be overcome by mapping between them using projective measurements. We have explicated the theory of projective measurements in a recent pedagogical article [29]. Subsequently, this raises the following questions: is it possible to utilize projective measurements as part of a many-body dynamical simulation method? Furthermore, is it possible to use such a method to implement large-scale simulations, thus opening the door to probing the efficacy of TQC on full quantum circuits? This is vital in justifying the platform and material parameters required to achieve fault tolerance in an experimental setting.

In this paper, we incorporate projective measurements into a general time-dependent superconducting many-particle formalism, allowing us to map between sparse and dense Majorana-qubit encodings (see Fig. 1), and thus to perform many-body simulations of TQC on more than two qubits, far beyond what has been previously demonstrated in the literature. We first demonstrate the dynamic preparation of the Bell state, and then expand this to prepare the maximally entangled Greenberger–Horne–Zeilinger (GHZ) state on $N = 5$ qubits. We emphasize both the utility, along

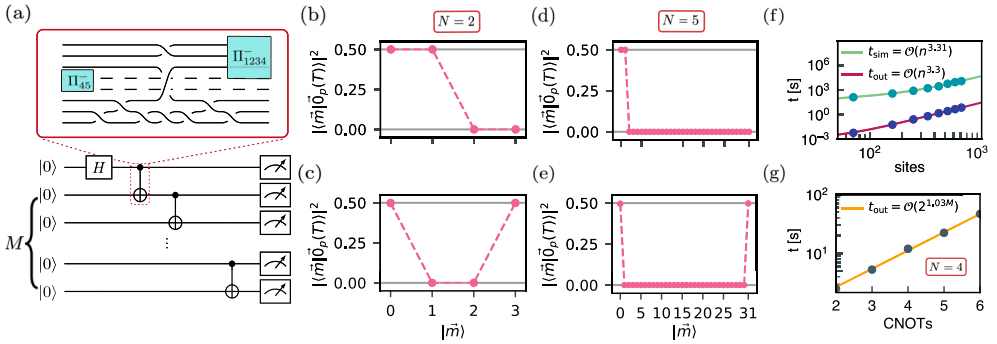


FIG. 2. N-qubit GHZ state preparation. (a) Circuit diagram of the GHZ state. (b), (c) Transition probabilities, $|T_{\vec{m}\vec{0}}(T)|^2$, of all qubit states for a two-qubit system, after a Hadamard on the first qubit [panel (b)] and a subsequent CNOT gate [panel (c)]. Qubit states are labeled as binaries; see main text. (d), (e) Same as panels (b) and (c) but for $N = 5$ GHZ state. (f) Average total readout time of a single overlap, $T_{\vec{0}\vec{0}}(T)$, after a single H gate on an N-sparse-qubit system. (g) Same as panel (f) but after M CNOTs for $N = 4$. Solid lines in panels (f) and (g) are fits as indicated by the legend. Parameters used are $(\tilde{t},\ \mu_{\text{topo}},\ \mu_{\text{triv}},\ |\Delta_p|,\ L) = (1, 0.02, 10.4, 0.98, 7a_0)$ for all simulations, with $T_{\text{braid}} = 2400\hbar/\tilde{t}$ for panels (b)–(e) and $T_{\text{braid}} = 1500\hbar/\tilde{t}$ for panels (f) and (g). Note that the dotted lines between data points in panels (b)–(e) are intended as a guide for the reader to highlight changes in the transition probability.

with the universality of the method, by the dynamic execution of a random unitary circuit on five qubits, matching the exact unitary with fidelity beyond 99%. Next, we explore the dependence of this fidelity on the total braid time T_{braid} and static potential disorder V. The resulting fidelity plot features extended areas of >99%, which shows that TQC is indeed immune to static disorder. Finally, we push the computational boundary and perform a random unitary circuit on $N = 10$ qubits, corresponding to 40 MZMs.

II. RESULTS

We will demonstrate the efficacy of utilizing this projection method to classically simulate a scalable quantum computer on MZM-based platforms. Each gate in this paper is performed dynamically, either through a set of braids ($\sqrt{X}$, S, CNOT) or through a timed MZM hybridization routine (T) [13]. A schematic of the braids required for a CNOT gate in the dense encoding [30], in the basis discussed in the Appendixes, is given schematically in Fig. 2(a). In addition, all time-dependent overlaps are calculated using the time-dependent Pfaffian method [16], an application of Hartree-Fock-Bogoliubov theory [31–33], and an exact method for finding arbitrary overlaps of many-body states in a free theory. Finally, all computational results were computed in the X basis [4], where for $k \in \{1, \ldots, N\}$, the computational Hilbert space is stabilized by the set of operators $\pm i\gamma_{4k-2}\gamma_{4k-1}$, $\pm i\gamma_{4k-3}\gamma_{4k}$. Here, γ_{4k-3} and γ_{4k+4} are projected out when moving to the dense encoding, retaining $\gamma_{4k-2}, \ldots, \gamma_{4k+2}$ in the dense encoding.

We will utilize the Kitaev chain system [9] for the creation of MZMs as it is the minimal model of topological superconductivity. The time-dependent Hamiltonian is given by

$$H(t) = -\sum_a \mu_a(t) c_a^\dagger c_a - \tilde{t}\sum_a \left(c_a^\dagger c_{a+1} + \text{H.c.}\right) - \sum_a \left(\Delta_p c_a^\dagger c_{a+1}^\dagger + \text{H.c.}\right), \tag{1}$$

where $\mu_a(t)$, $\tilde{t}$, and Δ_p correspond to a time-dependent potential term, tunneling strength, and p-wave superconducting pairing strength. Note that $\Delta_p = e^{i\phi}|\Delta_p|$, where $\phi \in [0, 2\pi]$. The topological regime, characterized by MZMs on the boundary, is specified when $|\mu| < 2\tilde{t}$. In this way, we may ramp the chemical potential locally between the topological (μ_{topo}) and trivial (μ_{triv}) regimes to spatially move the MZMs along the chain (See the Appendixes for further details on

the ramping protocol). By joining three chains in the form of three legs, with the pairing phase in the horizontal (vertical) legs $\phi = 0$ ($\phi = \frac{\pi}{2}$), we are able to form a T junction [34], the minimal structure required to braid two MZMs.

It is convenient to extend this model to a multi-T-junction geometry, where $2n-1$ such T junctions may then be joined together to construct a model that can braid $2n$ MZMs, with a single leg in between each neighboring set of MZMs. A schematic of the structure for two qubits is given in Fig. 1, with L the number of sites sandwiched between each initial MZM and the neighboring junction points of the structure, as well as the number of sites on each vertical leg.

Projective measurements map a logical two-qubit state from the sparse encoding, $|\vec{n}\rangle_s$, into the dense encoding, $|\vec{n}\rangle_d$ [29]. For simplicity, consider a set of Majorana bound states initialized in the $d_{2i-1,2i} = \frac{1}{2}(\gamma_{2i-1} + i\gamma_{2i})$ basis. A possible set of projection operators encoding the projective measurements are given by Π^-_{45} and Π^-_{1234}. These act on $|\vec{n}\rangle_s$ and $|\vec{n}\rangle_d$ as follows:

$$\Pi^-_{45}|\vec{n}\rangle_s = \frac{1}{\sqrt{2}}|\vec{n}\rangle_d, \quad \Pi^-_{1234}|\vec{n}\rangle_d = \frac{1}{\sqrt{2}}|\vec{n}\rangle_s. \tag{2}$$

Here, Π^-_{45} will project $|\vec{n}\rangle_s$ into the subspace where qubits 1 and 2 have even joint parity in γ_4 and γ_5, satisfying $-i\gamma_4\gamma_5|\vec{n}\rangle_d = |\vec{n}\rangle_d$. Subsequently, $|\vec{n}\rangle_d$ will also have even total parity; i.e., it will map to the subspace where the total occupation of the Fock state corresponds to an even number in the dense encoding. Subsequently, Π^-_{1234} projects the state back into the sparse encoding of total even parity. Vitally, this is done *without* a loss of quantum information, making this a nondestructive process. The explicit definitions for Π^-_{45} and Π^-_{1234}, along with their odd parity counterparts, are given in the Appendixes.

The advantages of utilizing this process are immediately evident. While all single-qubit gates may be safely implemented in the sparse encoding, we project into the dense encoding in order to enact any string of CZ and/or CNOT gates between two neighboring qubits, i.e., to entangle the qubits. We then project back onto the sparse encoding once we are finished with these two-qubit processes.

The implementation of projective measurements into the time-dependent Pfaffian method is then explicitly done by computing the transition matrix, $T_{\vec{m}\vec{n}}(t)$, given by

$$\begin{aligned} T_{\vec{m}\vec{n}}(t) &= 2\langle\vec{m}|U(t,t_2)\Pi^-_{1234}U(t_2,t_1)\Pi^-_{45}U(t_1,t_0)|\vec{n}\rangle \\ &= \langle\vec{m}|\vec{n}_p(t)\rangle, \end{aligned} \tag{3}$$

where $U(t_i,t_j)$ is the time-evolution operator. We denote the state $|\vec{n}_p(t)\rangle$ as the *projected state*, corresponding to the quantum state recovered after the application of both single- and two-qubit unitary time evolutions, along with the associated projective measurements required to enact these gates. More details on the projection operators Π^-_{45} and Π^-_{1234} as well as their *odd* parity counterparts, the transition matrix $T_{\vec{m}\vec{n}}(t)$, and time-evolution routine are provided in the Appendixes.

A. GHZ state and computational scaling

We begin with two qubits. First, we institute an H gate on the first qubit, mapping $|00\rangle \rightarrow \frac{1}{\sqrt{2}}(|00\rangle + |10\rangle)$, as demonstrated in Figs. 2(b) and 2(c). Using the projective method detailed in the previous paragraph, we map the quantum information from the sparse encoding to the dense encoding, where we can perform a CNOT gate, which maps $|10\rangle \rightarrow |11\rangle$, keeping $|00\rangle$ unaffected. This is shown in Figs. 2(b) and 2(c), which demonstrate a probability transfer from the $|10\rangle$ state to the $|11\rangle$ state, thus corresponding to the successful implementation of the projective method. We note that all logical states are indexed using a binary mapping f: $\mathcal{H} \rightarrow \mathbb{Z}$, where $f(|n_1, n_2, \ldots, n_N\rangle) = \sum_{i=0}^{N-1} 2^i n_{i+1}$ in the sparse encoding.

We then emphasize the scalability of the method by introducing the generalized GHZ state on N sparse qubits, with the definition $|\mathrm{GHZ}(N)\rangle = \frac{1}{\sqrt{2}}(|0\rangle^{\otimes_N} + |1\rangle^{\otimes_N})$, where, for an arbitrary state $|a\rangle$, $|a\rangle^{\otimes_M} = \bigotimes_{i=1}^{M} |a\rangle$. The corresponding circuit diagram required to produce this state from the initial

$|\vec{0}\rangle$ state is given in Fig. 2(a). After the first H gate, $|\vec{0}\rangle \to \frac{1}{\sqrt{2}}(|0\rangle + |1\rangle) \otimes |0\rangle^{\otimes_{N=4}}$, as shown in Fig. 2(d). A string of CNOT gates is then implemented on each pair of neighboring sparse qubits, as indicated schematically in Fig. 2(a). This maps the state to the generalized GHZ state on five qubits, defined by $|\vec{0}_p(T)\rangle = \frac{1}{\sqrt{2}}(|0\rangle^{\otimes_{N=5}} + |1\rangle^{\otimes_{N=5}}) = |\mathrm{GHZ}(5)\rangle$, as demonstrated in Fig. 2(e). Next, we investigate the computational scaling of the classical simulation method. This is highlighted in Figs. 1(f) and 1(g), where we track the average readout time as a function of N after a single-qubit gate [panel (f)], and then investigate how the readout time scales as a function of the projective operations [panel (g)]. In Fig. 1(f), we apply a single H gate on a system with N sparse qubits, with both sets of data fit against the number of lattice sites $n \equiv n(N) = 70 + 92(N-1)$. First, we consider the time required to construct the time-evolution operator $U(T, 0)$. Here, we find a polynomial scaling in the simulation time, with $t_{\mathrm{sim}} = [(0.024\, n)^{3.31} + 1.82\, n]$ s for $N \in [1, 9]$ after 50 simulations. We extend this analysis to the readout time of a single overlap, $T_{\vec{0}\vec{0}}(T)$. First, we note that the contraction matrix $M_{\vec{0}\vec{0}}(t)$, where $T_{\vec{0}\vec{0}}(T) \propto \mathrm{pf}[M_{\vec{0}\vec{0}}(T)]$, has size $2n - p$, with p corresponding to the size of the empty sector after the Bloch-Messiah decomposition (see Ref. [29] for further details). Assuming the empty sector to be small versus the size of the system (i.e., $2n \gg p$), which is consistent with our simulations, we fit the average time taken against n, thus providing a prediction for the readout time versus the physical parameter set utilized. Here, we find that the readout time scales as $t_{\mathrm{read}} = [(2.5 \times 10^{-3}\, n)^{3.30} + 4.6 \times 10^{-5}\, n]$ s $\sim \mathcal{O}(n^{3.3})$ in our dataset, approaching the expected $\mathcal{O}(n^3)$ scaling of the Pfaffian calculation [35], which dominates the routine in the large-n regime. Critically, while the total simulation time will increase linearly with the number of single-qubit gates implemented on top of this scaling, the readout time will remain the same, with the size of the system being the only determining factor. This is not the case when including projective measurements. For example, by setting $N = 4$, which fixes the number of lattice sites n, we replace the Hadamard gate with a string of CNOTs on the first qubit. As shown in Fig. 1(g), we find that the readout time scales as $t_{\mathrm{read}} = [0.64 \times 2^{1.03M}]$ s. This highlights the exponential increase in computational time with every projective operation, with M the number of times we map between the sparse and dense encodings, which corresponds exactly with the number of CNOT gates implemented. This is in line with the increase in the number of contractions required to find $T_{\vec{m}\vec{n}}(T)$, which increases as 2^M.

While we observe exponential scaling in the projective measurements, we highlight two vital points: First, we demonstrate how it is a feasible framework to perform large-scale braiding simulations for systems with N qubits. Second, each overlap in the output routine may, in essence, be calculated sequentially. This removes the cost of storing the full quantum state throughout the process, which will lead to an exponential scaling in data storage with the number of qubits in the system. Thus, the number of overlaps done in parallel may be optimized against both total CPU time and memory constraints, providing a malleable procedure to extract quantum information.

B. Random circuit

We now look to demonstrate the feasibility of the method to simulate any generic quantum computation. In this section, we will focus on the simulation of a random circuit, enacted on an $N = 5$-sparse-qubit system, with the circuit generated given in Fig. 3(a).

Further, we also consider the effects of static disorder on the system, thus emphasizing the utility of this method to probe the physical conditions of the underlying platform hosting MZMs. We do this by, at each point l on the adjoined T junction, adding an impurity term to the Hamiltonian of the form $w_l c_l^\dagger c_l$. Here, each on-site w_l is sampled from a uniform distribution spanning from $[-V, V]$, thus establishing a static disorder configuration that shifts the local energetics of the lattice structure. Each data point in Fig. 3 corresponds to a different effective disorder configuration, thereby providing a picture for the ensemble effect of the perturbation on the physics of large-scale MZM braiding. First, while disorder will perturb the energy landscape, thus affecting the timed hybridization routine necessary to implement the T gate, we overcome this issue by calibrating for

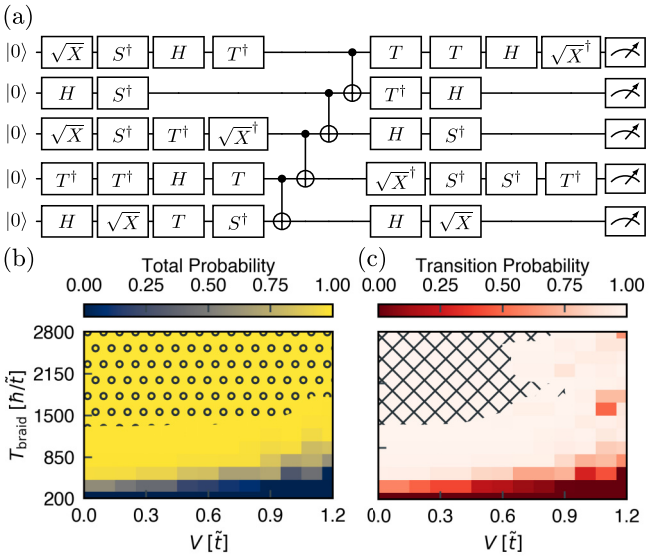


FIG. 3. Random unitary circuit in the presence of static disorder. (a) Schematic of the random unitary circuit. (b) Total probability within the MZM subspace, corresponding to $\sum_n |T_{\vec{n}\vec{0}}(T)|^2$. (c) Fidelity between the time-evolved projected state $|\vec{0}_p(T)\rangle$ and the corresponding target state $|t\rangle$, with regions of probability >99% highlighted by hatches overlaying the data. In panels (b) and (c), quantities are plotted as a function of braid time T_{braid} and disorder strength V. Parameters used in all simulations are $(\tilde{t},\ \mu_{\text{topo}},\ \mu_{\text{triv}},\ |\Delta_p|,\ L) = (1,\ 0.02,\ 8.8,\ 0.9,\ 8a_0)$.

the required time to implement the T gate on each Majorana bound state, before the implementation of the circuit, thus circumventing this issue. Next, as discussed in Ref. [23], for braiding, static disorder introduces two major error sources: *diabatic error* as the effective bulk gap is reduced in large V regimes, leading to an increased likelihood of loss of quantum information to the bulk, along with the potential for increased *hybridization error*, due to local impurities driving MZM wavefunction broadening. This leads to an increased likelihood of wavefunction overlap with other MZMs in the system, and thus unwanted SO($4N$) rotations of the MZM operators [17,29]. We reveal the effects of adiabatic error in Fig. 3(b), where the total probability measured in the ground-state manifold approaches 1 as the time of each braid T_{braid} approaches $2800\hbar/\tilde{t}$. This confirms the entering of the adiabatic regime in the large limit of T_{braid}, whereby the total state probability remains conserved with the ground-state manifold. However, as shown in Fig. 3(c), while the system is clearly in the adiabatic regime, as V increases, the system accrues error within the MZM subspace. For lower values of V, we see that these hybridization effects are diminished, leading to a stable region where the fidelity $|\langle t|\vec{0}_p(T)\rangle|^2 > 0.99$, regardless of the disorder configuration. In the case of large disorder strengths, we clearly demonstrate that these error sources remain detrimental to braiding, with no simulation satisfying a fidelity larger than 99% for disorder configurations with $V \geqslant \tilde{t}$.

In essence, we have demonstrated the scalability of the method to large circuits, while stressing the utility of the method to investigate the effects of various error sources on large quantum circuits.

C. Large-scale simulation of a quantum circuit

Finally, we extend this by simulating a random unitary circuit on a large-scale ten-qubit system, where we again perform a CNOT gate on each neighboring pair of qubits, sandwiched in between a randomly chosen set of single-qubit gates. A schematic of the circuit is given in Fig. 4. In total, it

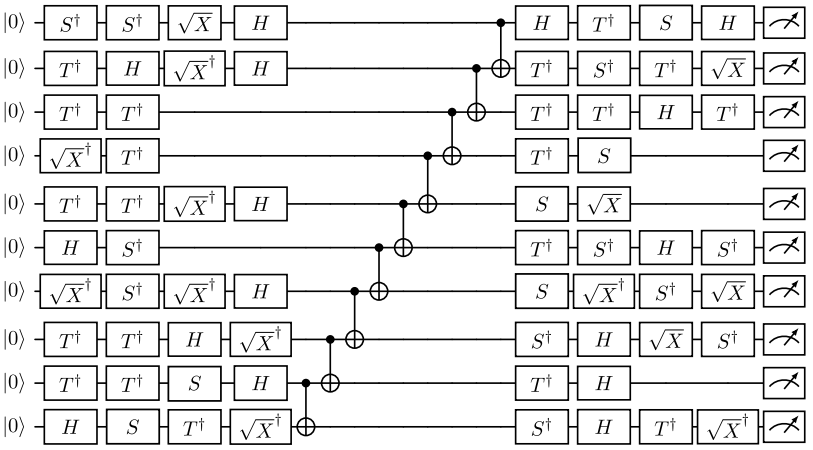


FIG. 4. Schematic of the quantum circuit utilized for the ten-qubit simulation.

contains 77 qubit gates enacted on the circuit, with 18 projective measurements, corresponding to $M = 9$.

We consider the matrix elements of the projected overlap $T_{\vec{i}\vec{0}}(T)$. This is shown in Fig. 5, where the absolute values of the matrix elements are plotted against the magnitudes of the target state associated with this random circuit. Moreover, while Fig. 5 removes phase information, providing an incomplete picture of the distance between the projected and final states, we see that the fidelity, while dipping below the threshold fidelity of 99%, as discussed in Fig. 3, remains significant, with $|\langle t|\vec{0}_p(T)\rangle|^2 = 0.974$, with the total probability of the time-evolved state being $\sum_i |T_{\vec{i}\vec{0}}(T)|^2 = 0.981$. This suggests that while probability is lost as a result of diabatic and hybridization errors, marginally deviating the result away from the target state, the non-Abelian braiding statistics is preserved over the course of the simulation. As such, this stands as a successful simulation of a ten-qubit quantum circuit on an MZM platform, and demonstrative of the largest simulation of any topological quantum circuit on an MZM-based platform.

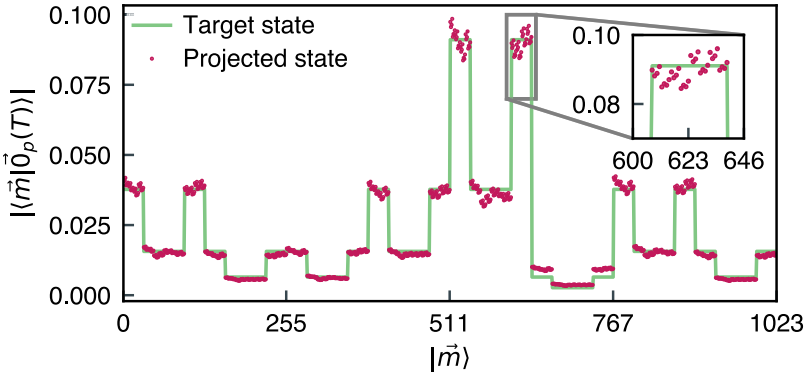


FIG. 5. Transition probabilities for ten-qubit simulation of a random unitary. Parameters used in this simulations are $(\tilde{t},\ \mu_{\text{topo}},\ \mu_{\text{triv}},\ |\Delta_p|,\ L, T_{\text{braid}}) = (1,\ 0.02,\ 10.4,\ 0.98,\ 7a_0, 2000\hbar/\tilde{t})$.

III. DISCUSSION

We have shown that projective measurements not only stand as a potential pathway toward universal topological quantum computation, but by extending the scalable method introduced in Ref. [16], this method opens the door for the classical simulation of large-scale quantum circuits within this particular paradigm. In particular, this has allowed us to perform TQC simulations for more than two qubits for the first time.

Although all results have been found using the spinless Kitaev nanowire model, we stress that the method is fundamentally platform independent. As such, there is scope for future investigation on superconductor-semiconductor heterostructures [36–39], magnetic superconductor hybrid systems [15,40–44], and two-dimensional higher-order platforms [45,46], all of which provide scalable platforms for MZM braiding and are eminently realizable experimentally.

While we have chosen beneficial parameter sets to demonstrate the recovery of the non-Abelian statistical properties of the MZMs, as shown in Fig. 3, this method opens the door to investigate real-world conditions and various sources of error on quantum circuits. Finally, we stress that by calculating each overlap sequentially we avoid the cost of storing the full quantum state over the course of the readout, which grows exponentially with the number of qubits.

In conclusion, we have detailed an accessible procedure for performing large-scale simulations with Majorana zero modes. It provides access to numerical experiments, thus informing physical circuit production in the pursuit of TQC.

ACKNOWLEDGMENTS

S.R. acknowledges discussions with Sankar das Sarma, Bela Bauer, and Cole Peeters. The authors are grateful to Eric Mascot for closely related collaborations. This work was supported by the Australian Research Council (ARC) through Grant No. DP240100168. This research was undertaken using resources from the National Computational Infrastructure (NCI Australia), an NCRIS-enabled facility supported by the Australian Government. The authors gratefully acknowledge the scientific support and HPC resources provided by the Erlangen National High Performance Computing Center (NHR@FAU) of the Friedrich-Alexander-Universität Erlangen-Nürnberg (FAU) under the NHR project "k102de–FRG." NHR funding is provided by federal and Bavarian state authorities. NHR@FAU hardware is partially funded by the DFG—440719683.

DATA AVAILABILITY

The data that support the findings of this article are openly available [47].

APPENDIX A: TIME-DEPENDENT RAMPING PROTOCOL

On a given leg, the on-site chemical potential $\mu_i(t)$ is locally ramped between a topological (μ_{topo}) and a trivial (μ_{triv}) choice if parametrized via a *polynomial ramp protocol* [16,48]. On a given leg, with sites now parametrized between $i = 1$ (leftmost site) and $i = L$ (rightmost site), the ramping protocol is given by

$$\mu_i(t) = \mu_{\text{triv}} + (\mu_{\text{topo}} - \mu_{\text{triv}})\, s\left(\frac{t}{\tau}(1 + \alpha(N-1)) - \alpha i\right). \tag{A1}$$

Here, the function $s : \mathbb{R} \to \mathbb{R}$ denotes a polynomial step function, parametrized as follows:

$$s(q) = \begin{cases} 0, & q \leqslant 0, \\ q^2(3-2q), & 0 \leqslant q \leqslant 1, \\ 1, & 1 \leqslant q. \end{cases} \tag{A2}$$

In this case, at $s(q) = 0$, the site is at $\mu_i = \mu_{\text{triv}}$ and for $s(q) = 1$, $\mu_i = \mu_{\text{topo}}$, with intermediate values interpolating between these two outcomes. As such, this site-dependent ramp will spatially

move the MZMs across the leg, allowing for their spatial exchange on the adjoined T-junction structure. For all simulations, $\alpha = 0.025$.

APPENDIX B: THE PFAFFIAN METHOD

We now describe the method with which all overlap functions are calculated, utilizing the time-dependent Pfaffian method introduced in Ref. [16].

First, at $t = 0$, the Hamiltonian may also be written in its *diagonal representation* spanned by bilinears $d_k^\dagger d_k$ of the set of Bogoliubov quasiparticles, $\{d_k\}$. This is given by

$$H(0) = \sum_{k=1}^{M} E_k \left(d_k^\dagger d_k - \frac{1}{2} \right), \tag{B1}$$

where all energies $E_k \geqslant 0$ for all k, and the set of electron operators $\{c_a\}$ are mapped to $\{d_k\}$ by a *Bogoliubov transformation* given by

$$\begin{pmatrix} c \\ c^\dagger \end{pmatrix} = \begin{pmatrix} U & V^* \\ V & U^* \end{pmatrix} \begin{pmatrix} d \\ d^\dagger \end{pmatrix}, \tag{B2}$$

where $c = (c_1,\ c_2, \ldots,\ c_N)^T$ and $d(t) = (d_1(t),\ d_2(t), \ldots,\ d_N(t))^T$, with $d_i(0) \equiv d_i$.

Using the set of Bogoliubov quasiparticles, we define a natural choice of basis for the many-body Hilbert space, being the *Fock space*, constructed out of Bogoliubov quasiparticles:

$$|\vec{n}\rangle = \prod_k (d_k^\dagger)^{n_k} |\vec{0}_d\rangle. \tag{B3}$$

Here, $|\vec{0}_d\rangle$ corresponds to the *Bogoliubov vacuum*, defined such that $d_k|\vec{0}_d\rangle = 0\ \forall\ k$, with $n_k = 0\,(1)$ indexing that the state is empty (occupied).

We will map the c_a, d_k operators to their *canonical forms* via $\bar{c}_a$, $\bar{d}_k$ using a *Bloch-Messiah decomposition* [31,49], given by

$$c_a = \sum_b C_{ab} \bar{c}_b, \quad d_k = \sum_j D_{kl} \bar{d}_l. \tag{B4}$$

Matrices C and D correspond to unitary matrices, and additionally decompose the U and V matrices in the Bogoliubov transformation defined in Eq. (D5) by $U = C\bar{U}D^\dagger$ and $V = C^*\bar{V}D^\dagger$. Utilizing this transformation, the Fock state provided in Eq. (B3) is given by

$$|\vec{n}\rangle = \prod_k (d_k^\dagger)^{n_k} \frac{1}{\sqrt{\mathcal{N}}} \prod_{k\in P} \bar{d}_k \bar{d}_{\bar{k}} \prod_{k\in O} \bar{d}_k |\vec{0}_c\rangle, \tag{B5}$$

where $|\vec{0}_c\rangle$ is the bare fermionic vacuum, defined such that $c_k|\vec{0}_c\rangle = 0\ \forall\ k$. The forms for $\bar{U}$ and $\bar{V}$ are given by

$$\bar{U} = \begin{pmatrix} I & & \\ & \oplus_k u_k \sigma_0 & \\ & & 0 \end{pmatrix}, \quad \bar{V} = \begin{pmatrix} 0 & & \\ & \oplus_k v_k i\sigma_y & \\ & & I \end{pmatrix}, \tag{B6}$$

where $u_k,\ v_k \in \mathbb{R}$, and $u_k^2 + v_k^2 = 1$. The zero, middle, and identity blocks of the $\bar{V}$ matrix are denoted as the *empty*, *paired*, and *occupied* sectors, respectively, with indices segmenting each sector labeled by $E,\ P,\ O$. Further, each tuple $(k, \bar{k})$ corresponds to a pairing of indices in the paired sector of same v_k. The transformation is performed to remove $\bar{d}_k$ operators associated with the empty sector, which will annihilate the vacuum, thus removing numerical instabilities from the calculation. Finally, the normalization factor $\mathcal{N} = \prod_{k\in P} v_k^2$.

Overlaps between arbitrary Fock states and any string of operators $\mathcal{A}$ may be arbitrarily calculated by an application of Wick's theorem [32,50,51]. For an arbitrary state $|m'\rangle = \prod_k (d_k'^{\dagger})^{m_k'}|0_{d'}\rangle$, with $m_k' \in \{0, 1\}$ labeling the occupancy of the state and $|0_{d'}\rangle$ the Bogoliubov vacuum constructed from the set $\{d_k'\}$, up to a global $U(1)$ gauge factor, any generic overlap is given by

$$\langle \vec{m}'|\mathcal{A}|\vec{n}\rangle = \frac{s_{\vec{m}'}}{\sqrt{\mathcal{N}'\mathcal{N}}}\mathrm{pf}\begin{pmatrix} \overbrace{\bar{d}'^{\dagger}\bar{d}'^{\dagger}} & \overbrace{\bar{d}'^{\dagger}d'} & \overbrace{\bar{d}'^{\dagger}\mathcal{A}} & \overbrace{\bar{d}'^{\dagger}d^{\dagger}} & \overbrace{\bar{d}'^{\dagger}\bar{d}} \\ & \overbrace{d'd'} & \overbrace{d'\mathcal{A}} & \overbrace{d'd^{\dagger}} & \overbrace{d'\bar{d}} \\ & & \overbrace{\mathcal{A}\mathcal{A}} & \overbrace{\mathcal{A}d^{\dagger}} & \overbrace{\mathcal{A}\bar{d}} \\ & & & \overbrace{d^{\dagger}d^{\dagger}} & \overbrace{d^{\dagger}\bar{d}} \\ & & & & \end{pmatrix}, \tag{B7}$$

with $s_{\vec{m}'} = (-1)^{\sum_k m_k'(\sum_k m_k'-1)/2}$ due to the reversal of operator order in $\langle\vec{m}'|$. Additionally, each $\overbrace{ab}$ sector denotes the matrix of contractions such that $[\overbrace{ab}]_{ij} = \langle\vec{0}_c|a_i b_j|\vec{0}_c\rangle$. Finally, all empty elements in the lower triangle of the matrix are gained via the antisymmetry of the matrix.

APPENDIX C: PROJECTIVE MEASUREMENTS

As discussed in the Introduction, and in detail in Ref. [29], for the purpose of scalable quantum computation, projective measurements between sparse and dense encodings are a viable pathway toward the implementation of a universal gate set. A schematic of both is shown in Fig. 1. In essence, this method relies on the projection of a logical two-qubit state in the sparse encoding, $|\vec{n}\rangle_s$, into the dense encoding, $|\vec{n}\rangle_d$. In general, the system may be initialized with respect to an arbitrary pairing of the MZM operators, amounting to a basis choice; for this discussion, we consider a set of Majorana bound states initialized in the $d_{2i-1,2i} = \frac{1}{2}(\gamma_{2i-1} + i\gamma_{2i})$ basis, in line with the discussion in Ref. [29]. For simplicity, we focus on a discussion of the two-qubit system, composed of eight MZMs in the sparse encoding, and note that this argument is generalized to N-qubit systems by simply using the same procedure on the set of MZMs involved in the projective measurement routine. A set of projection operators encoding the projective measurements are given by

$$\Pi_{45}^{\mp} = \tfrac{1}{2} \mp \tfrac{1}{2} \pm d_{45}d_{45}^{\dagger}, \quad \Pi_{1234}^{\mp} = \tfrac{1}{2}(1 \pm Q_{s,1}), \tag{C1}$$

where $Q_{s,1} = -\gamma_1\gamma_2\gamma_3\gamma_4$ is the total parity of the first qubit in the sparse encoding. For a two-qubit system with both sparse qubits in the even (odd) parity subspace, it will satisfy $Q_{s,1}|\vec{n}\rangle_s = |\vec{n}\rangle_s$ $(-|\vec{n}\rangle_s)$. Its dense encoding counterpart Q_d is given by $Q_d = i\gamma_1\gamma_2\gamma_3\gamma_6\gamma_7\gamma_8$, which calculates the total parity of the two-qubit system. Similarly to Q_d, a dense qubit encoded in the even (odd) parity subspace will satisfy $Q_d|\vec{n}\rangle_d = |\vec{n}\rangle_d$ $(-|\vec{n}\rangle_d)$.

Here, the projection operator Π_{45}^{-} (Π_{45}^{+}) will project the state into the subspace where qubits 1 and 2 have even (odd) joint parity in $-i\gamma_4\gamma_5$. This projection is made possible via MZM fusion of γ_4 and γ_5, which will measure the parity sector of the $-i\gamma_4\gamma_5$ bound state. Subsequently, Π_{1234}^{-} (Π_{1234}^{+}) projects the state back into the sparse encoding of total even (odd) parity. Without loss of generality, we define both $|\vec{n}\rangle_s$ and $|\vec{n}\rangle_d$ in the even parity subspace. In this case, we recover the result in Eq. (2), i.e.,

$$\Pi_{45}^{-}|\vec{n}\rangle_s = \frac{1}{\sqrt{2}}|\vec{n}\rangle_d, \quad \Pi_{1234}^{-}|\vec{n}\rangle_d = \frac{1}{\sqrt{2}}|\vec{n}\rangle_s. \tag{C2}$$

We stress that equivalently we may project into the subspace of odd joint parity, without any loss of quantum information. The advantages of utilizing this process are immediately evident. While all single-qubit gates may be safely implemented in the sparse encoding, we project into the dense encoding in order to enact any string of CZ and/or CNOT gates between two neighboring qubits, i.e., to entangle the qubits. We then project back onto the sparse encoding once we are finished with these two-qubit processes.

APPENDIX D: TIME-DEPENDENT SIMULATION OF A TOPOLOGICAL QUANTUM COMPUTER

We will now introduce the methodology utilized for the time-dependent simulation and stress *how* we incorporate projective measurements to enable scalable simulation of TQC on any platform.

To begin with, we define the *time-evolved Fock state*, given by

$$|\vec{n}(t)\rangle = \prod_k (d_k^\dagger(t))^{n_k} |\vec{0}_d(t)\rangle. \tag{D1}$$

This is just an adaption of the form introduced in Eq. (B3), where we apply the *time-evolution operator*, $U(t,0)$, given by

$$U(t_i,t_j) = \mathcal{T}\exp\left(-i\int_{t_j}^{t_i} H(t')dt'\right). \tag{D2}$$

Here, $\mathcal{T}$ is the *time-ordering operator*, defined such that, for two operators $A(t_1)$, $B(t_2)$, the time-ordered product between the two is given by

$$\mathcal{T}(A(t_i)B(t_j)) = \begin{cases} A(t_i)B(t_j), & t_i > t_j, \\ B(t_j)A(t_i), & t_j > t_i. \end{cases} \tag{D3}$$

Further, each time-evolved quasiparticle operator, $d_k(t)$, is defined by

$$d_k(t) = U(t,0)d_k U^\dagger(t,0). \tag{D4}$$

For the purpose of calculation, we note the connection between the bare fermionic operators, c_a, and the time-evolved Bogoliubov quasiparticles, $d_k(t)$, given by

$$\begin{pmatrix} c \\ c^\dagger \end{pmatrix} = \begin{pmatrix} U(t) & V(t)^* \\ V(t) & U(t)^* \end{pmatrix} \begin{pmatrix} d(t) \\ d^\dagger(t) \end{pmatrix}, \tag{D5}$$

where the time-evolved Bogoliubov transformation matrix is derived from the *time-dependent Bogoliubov-de Gennes equation* [17,52,53], given by

$$i\partial_t \begin{pmatrix} U(t) & V(t)^* \\ V(t) & U(t)^* \end{pmatrix} = H_{\mathrm{BdG}}(t) \begin{pmatrix} U(t) & V(t)^* \\ V(t) & U(t)^* \end{pmatrix}. \tag{D6}$$

We are now in a position to read out quantum information from the simulation process. We begin with a quantum circuit featuring a single sparse-to-dense projection protocol on two sparse qubits. As introduced in Eq. (3), for the purpose of classical simulation, we read the quantum information by finding the transition matrix, $T_{\vec{m}\vec{n}}(t)$, given by

$$\begin{aligned} T_{\vec{m}\vec{n}}(t) &= 2\langle \vec{m}|U(t,t_2)\Pi^-_{1234}U(t_2,t_1)\Pi^-_{45}U(t_1,t_0)|\vec{n}\rangle \\ &= \langle \vec{m}|\vec{n}_p(t)\rangle. \end{aligned} \tag{D7}$$

Here, $U(t,t_2)$ and $U(t_1,t_0)$ correspond to the time evolution associated with single-qubit processes in sparse encoding, and $U(t_2,t_1)$ with two-qubit gates in dense encoding, with the normalization factor $\sqrt{2}$ required to conserve total probability. Here, the projected state is defined by

$$|\vec{n}_p(t)\rangle = 2 \times \Pi^-_{1234}(t,t_2)\Pi^-_{45}(t,t_1)|\vec{n}(t)\rangle, \tag{D8}$$

with the operators $\Pi^-_{1234}(t_a,t_b)$ and $\Pi^-_{45}(t_a,t_b)$ given by

$$\Pi^-_{45}(t_b,t_a) = d_{45}(t_b,t_a)d^\dagger_{45}(t_b,t_a), \tag{D9}$$

$$\Pi^-_{1234}(t_b,t_a) = \tfrac{1}{2}(1 + Q_{s,1}(t_b,t_a)), \tag{D10}$$

where $Q_{s,1}(t_b, t_a) = U(t_b, t_a)Q_{s,1}U^\dagger(t_b, t_a)$ and $d_{ij}(t_b, t_a) = U(t_b, t_a)d_{ij}U^\dagger(t_b, t_a)$. As such, by calculating $T_{\vec{m}\vec{n}}(T)$, with T the total simulation time, we recover all quantum information of the final state $|\vec{n}_p(T)\rangle$. Further, each contraction in Eq. (D7) is calculated, up to a global gauge factor, using the formula in Eq. (B7). As discussed in Sec. II, and found in Fig. 2(f), this calculation scales in polynomial time, versus the exponential size of the many-body Hilbert space:

$$\begin{aligned} T_{\vec{m}\vec{n}}(t) &= 2^M \langle \vec{m}|\mathcal{T}\left(\prod_{j=1}^{M} \Pi^-_{1234}(t, t_{2j})\Pi^-_{45}(t, t_{2j-1})\right)|\vec{n}(t)\rangle \\ &= \langle \vec{m}|\vec{n}_p(t)\rangle. \end{aligned} \tag{D11}$$

In this case, the overlap decomposes into 2^M contractions, thus introducing an exponential scaling in the number of calculations versus the number of contractions required to recover all quantum information. Although equations have been restricted to two qubits, as has been done in Sec. II, This is naturally expanded to N-qubit systems, with each projective measurement operator indexing the coupling between qubits involved in the sparse-to-dense mapping. This is done as follows:

$$\begin{aligned} T_{\vec{m}\vec{n}}(t) &= 2^M \langle \vec{m}|\mathcal{T}\left[\prod_{j=1}^{M} \Pi^-_{(4\sigma_1^j-3)(4\sigma_1^j-2)(4\sigma_1^j-1)(4\sigma_1^j)}(t, t_{2j})\Pi^-_{4\sigma_1^j(4\sigma_2^j-3)}(t, t_{2j-1})\right]|\vec{n}(t)\rangle \\ &= \langle \vec{m}|\mathcal{T}\left[\prod_{j=1}^{M}\sum_{n_j=0}^{1}\left(Q_{s,\sigma_1^j}(t, t_{2j})\right)^{n_j} d_{4\sigma_1^j(4\sigma_2^j-3)}(t, t_{2j-1})d^\dagger_{4\sigma_1^j(4\sigma_2^j-3)}(t, t_{2j-1})\right]|\vec{n}(t)\rangle \\ &= \langle \vec{m}|\vec{n}_p(t)\rangle. \end{aligned} \tag{D12}$$

The vector $\vec{\sigma}^j = (\sigma_1^j, \sigma_2^j)$, with $\sigma_i^j \in \{1, \ldots, N\}$, indexes which sparse qubits are coupled in the jth projective mapping process between the sparse and dense encodings. For the purpose of this paper, we restrict all projective measurements to neighboring qubits, but stress that this is not a restriction to the methodology. Thus, projective measurements provide an accessible and scalable method to perform large-scale quantum circuit simulation on MZM platforms.

[1] C. Nayak and F. Wilczek, $2n$-quasihole states realize 2^{n-1}-dimensional spinor braiding statistics in paired quantum Hall states, Nucl. Phys. B **479**, 529 (1996).

[2] D. A. Ivanov, Non-Abelian statistics of half-quantum vortices in p-wave superconductors, Phys. Rev. Lett. **86**, 268 (2001).

[3] L. S. Georgiev, Topologically protected gates for quantum computation with non-Abelian anyons in the Pfaffian quantum Hall state, Phys. Rev. B **74**, 235112 (2006).

[4] C. Nayak, S. H. Simon, A. Stern, M. Freedman, and S. Das Sarma, Non-Abelian anyons and topological quantum computation, Rev. Mod. Phys. **80**, 1083 (2008).

[5] P. Bonderson, V. Gurarie, and C. Nayak, Plasma analogy and non-Abelian statistics for Ising-type quantum Hall states, Phys. Rev. B **83**, 075303 (2011).

[6] M. Barkeshli, C.-M. Jian, and X.-L. Qi, Twist defects and projective non-Abelian braiding statistics, Phys. Rev. B **87**, 045130 (2013).

[7] C. W. J. Beenakker, Search for non-Abelian Majorana braiding statistics in superconductors, SciPost Phys. Lect. Notes 15 (2020).

[8] V. Lahtinen and J. K. Pachos, A short introduction to topological quantum computation, SciPost Phys. **3**, 021 (2017).

[9] A. Y. Kitaev, Unpaired Majorana fermions in quantum wires, Phys. Usp. **44**, 131 (2001).

[10] S. D. Sarma, M. Freedman, and C. Nayak, Majorana zero modes and topological quantum computation, npj Quantum Inf. **1**, 15001 (2015).

[11] P. Bonderson, D. J. Clarke, C. Nayak, and K. Shtengel, Implementing arbitrary phase gates with Ising anyons, Phys. Rev. Lett. **104**, 180505 (2010).
[12] T. Karzig, Y. Oreg, G. Refael, and M. H. Freedman, Universal geometric path to a robust Majorana magic gate, Phys. Rev. X **6**, 031019 (2016).
[13] T. Hodge, E. Mascot, D. Crawford, and S. Rachel, Characterizing dynamic hybridization of Majorana zero modes for universal quantum computing, Phys. Rev. Lett. **134**, 096601 (2025).
[14] T. Sanno, S. Miyazaki, T. Mizushima, and S. Fujimoto, *Ab initio* simulation of non-Abelian braiding statistics in topological superconductors, Phys. Rev. B **103**, 054504 (2021).
[15] J. Bedow, E. Mascot, T. Hodge, S. Rachel, and D. K. Morr, Simulating topological quantum gates in two-dimensional magnet-superconductor hybrid structures, npj Quantum Mater. **9**, 99 (2024).
[16] E. Mascot, T. Hodge, D. Crawford, J. Bedow, D. K. Morr, and S. Rachel, Many-body Majorana braiding without an exponential Hilbert space, Phys. Rev. Lett. **131**, 176601 (2023).
[17] M. Cheng, V. Galitski, and S. Das Sarma, Nonadiabatic effects in the braiding of non-Abelian anyons in topological superconductors, Phys. Rev. B **84**, 104529 (2011).
[18] T. Karzig, G. Refael, and F. von Oppen, Boosting Majorana zero modes, Phys. Rev. X **3**, 041017 (2013).
[19] M. S. Scheurer and A. Shnirman, Nonadiabatic processes in Majorana qubit systems, Phys. Rev. B **88**, 064515 (2013).
[20] C. Knapp, M. Zaletel, D. E. Liu, M. Cheng, P. Bonderson, and C. Nayak, The nature and correction of diabatic errors in anyon braiding, Phys. Rev. X **6**, 041003 (2016).
[21] P. W. Brouwer, M. Duckheim, A. Romito, and F. von Oppen, Probability distribution of Majorana end-state energies in disordered wires, Phys. Rev. Lett. **107**, 196804 (2011).
[22] B. P. Truong, K. Agarwal, and T. Pereg-Barnea, Optimizing the transport of Majorana zero modes in one-dimensional topological superconductors, Phys. Rev. B **107**, 104516 (2023).
[23] C. Peeters, T. Hodge, E. Mascot, and S. Rachel, Effect of impurities and disorder on the braiding dynamics of Majorana zero modes, Phys. Rev. B **110**, 214506 (2024).
[24] H. Pan and S. Das Sarma, Disordered Majorana nanowires: Studying disorder without any disorder, Phys. Rev. B **110**, 075401 (2024).
[25] J. Aumentado, M. W. Keller, J. M. Martinis, and M. H. Devoret, Nonequilibrium quasiparticles and 2e periodicity in single-Cooper-pair transistors, Phys. Rev. Lett. **92**, 066802 (2004).
[26] A. Bespalov, M. Houzet, J. S. Meyer, and Y. V. Nazarov, Theoretical model to explain excess of quasiparticles in superconductors, Phys. Rev. Lett. **117**, 117002 (2016).
[27] T. Karzig, C. Knapp, R. M. Lutchyn, P. Bonderson, M. B. Hastings, C. Nayak, J. Alicea, K. Flensberg, S. Plugge, Y. Oreg, C. M. Marcus, and M. H. Freedman, Scalable designs for quasiparticle-poisoning-protected topological quantum computation with Majorana zero modes, Phys. Rev. B **95**, 235305 (2017).
[28] T. Karzig, W. S. Cole, and D. I. Pikulin, Quasiparticle poisoning of Majorana qubits, Phys. Rev. Lett. **126**, 057702 (2021).
[29] P. Frey, T. Hodge, E. Mascot, and S. Rachel, Majorana braiding simulations with projective measurements, Phys. Rev. B **113**, 115153 (2026).
[30] L. S. Georgiev, Towards a universal set of topologically protected gates for quantum computation with Pfaffian qubits, Nucl. Phys. B **789**, 552 (2008).
[31] P. Ring and P. Schuck, *The Nuclear Many-Body Problem* (Springer, Heidelberg, 1980), 1st ed.
[32] G. F. Bertsch and L. M. Robledo, Symmetry restoration in Hartree-Fock-Bogoliubov based theories, Phys. Rev. Lett. **108**, 042505 (2012).
[33] B. G. Carlsson and J. Rotureau, New and practical formulation for overlaps of Bogoliubov vacua, Phys. Rev. Lett. **126**, 172501 (2021).
[34] J. Alicea, Y. Oreg, G. Refael, F. von Oppen, and M. P. A. Fisher, Non-Abelian statistics and topological quantum information processing in 1D wire networks, Nat. Phys. **7**, 412 (2011).
[35] M. Wimmer, Algorithm 923: Efficient numerical computation of the Pfaffian for dense and banded skew-symmetric matrices, ACM Trans. Math. Software **38**, 1 (2012).
[36] T. Karzig, Y. Oreg, G. Refael, and M. H. Freedman, Robust Majorana magic gates via measurements, Phys. Rev. B **99**, 144521 (2019).

[37] H. Pan and S. Das Sarma, Physical mechanisms for zero-bias conductance peaks in Majorana nanowires, Phys. Rev. Res. **2**, 013377 (2020).
[38] M. Aghaee *et al.* (Microsoft Quantum), InAs-Al hybrid devices passing the topological gap protocol, Phys. Rev. B **107**, 245423 (2023).
[39] M. Aghaee *et al.* (Microsoft Quantum Azure), Interferometric single-shot parity measurement in InAs–Al hybrid devices, Nature (London) **638**, 651 (2025).
[40] S. Nadj-Perge, I. K. Drozdov, B. A. Bernevig, and A. Yazdani, Proposal for realizing Majorana fermions in chains of magnetic atoms on a superconductor, Phys. Rev. B **88**, 020407 (2013).
[41] M. Ruby, F. Pientka, Y. Peng, F. von Oppen, B. W. Heinrich, and K. J. Franke, End states and subgap structure in proximity-coupled chains of magnetic adatoms, Phys. Rev. Lett. **115**, 197204 (2015).
[42] R. Pawlak, M. Kisiel, J. Klinovaja, T. Meier, S. Kawai, T. Glatzel, D. Loss, and E. Meyer, Probing atomic structure and Majorana wavefunctions in mono-atomic Fe chains on superconducting Pb surface, npj Quantum Inf. **2**, 16035 (2016).
[43] S. Rachel and R. Wiesendanger, Majorana quasiparticles in atomic spin chains on superconductors, Phys. Rep. **1099**, 1 (2025).
[44] T. Hodge, T. Kieu, J. Bedow, E. Mascot, D. K. Morr, and S. Rachel, Fusion dynamics of Majorana zero modes, Phys. Rev. B **113**, 035429 (2026).
[45] S.-B. Zhang, W. B. Rui, A. Calzona, S.-J. Choi, A. P. Schnyder, and B. Trauzettel, Topological and holonomic quantum computation based on second-order topological superconductors, Phys. Rev. Res. **2**, 043025 (2020).
[46] T. Hodge, E. Mascot, and S. Rachel, Altermagnet–superconductor heterostructure: A scalable platform for braiding of Majorana modes, APS Open Sci. **1**, L000045 (2026).
[47] T. Hodge, P. Frey, and S. Rachel, Projective measurements: Topological quantum computing with an arbitrary number of qubits [Dataset], Zenodo, 2026, https://doi.org/10.5281/zenodo.21385943.
[48] M. Sekania, S. Plugge, M. Greiter, R. Thomale, and P. Schmitteckert, Braiding errors in interacting Majorana quantum wires, Phys. Rev. B **96**, 094307 (2017).
[49] C. Bloch and A. Messiah, The canonical form of an antisymmetric tensor and its application to the theory of superconductivity, Nucl. Phys. **39**, 95 (1962).
[50] S. B. Bravyi and A. Y. Kitaev, Fermionic quantum computation, Ann. Phys. **298**, 210 (2002).
[51] L. M. Robledo, Sign of the overlap of Hartree-Fock-Bogoliubov wave functions, Phys. Rev. C **79**, 021302 (2009).
[52] A. F. Andreev, The thermal conductivity of the intermediate state in superconductors, J. Exptl. Theoret. Phys. (USSR) **46**, 1823 (1964) [Sov. Phys. JETP **19**, 1228 (1964)].
[53] R. Kümmel, Dynamics of current flow through the phase-boundary between a normal and a superconducting region, Z. Phys. **218**, 472 (1969).